EVALUATION OF THE SST-SAS MODEL: CHANNEL FLOW, ASYMMETRIC DIFFUSER AND AXI-SYMMETRIC HILL

Lars Davidson

Division of Fluid Dynamics, Department of Applied Mechanics
Chalmers University of Technology, SE-412 96 Göteborg, Sweden
e-mail: lada@chalmers.se

Key words: von Karman length scale, unsteady, URANS, DES, LES, scale-adapted

Abstract. *The SAS model (Scale Adapted Simulation) was invented by Menter and co-workers. The idea behind the SST-SAS $k - \omega$ model is to add an additional production term – the SAS term – in the ω equation, which is sensitive to resolved (i.e. unsteady) fluctuations. When the flow equations resolve turbulence, the length scale based on velocity gradients is much smaller than that based on time-averaged velocity gradients. Hence the von Kármán length scale, L_{vK}, is an appropriate quantity to use as a sensor for detecting unsteadiness. In regions where the flow is on the limit of going unsteady, the objective of the SAS term is to increase ω. The result is that k and ν_t are reduced so that the dissipating (damping) effect of the turbulent viscosity on the resolved fluctuations is reduced, thereby promoting the momentum equations to switch from steady to unsteady mode.*

The SST-SAS model and the standard SST-URANS are evaluated for three flows: developing channel flow, the flow in an asymmetric, plane diffuser and the flow around a three-dimensional axi-symmetric hill. Unsteady inlet boundary conditions are prescribed in all cases by superimposing turbulent fluctuations on a steady inlet boundary velocity profile.

1 Introduction

RANS turbulence models, such as two-equation eddy-viscosity models, are highly dissipative. This means that they are not likely to be triggered into unsteady mode unless the flow instabilities are strong (such as vortex shedding behind bluff bodies [1–3]). It is a good idea in many flow situations to let the RANS solution go unsteady. First, on a fine mesh, it may well be that no steady solution exists. In that case there is no point in trying to force the flow to a steady solution. Second, if some large movements (either the very largest turbulence structures or some quasi-periodic non-turbulent structure) are allowed to be resolved, the flow will be more accurately captured. In a way, this is the idea of DES [4, 5], in which the turbulence in the boundary layers is modelled (RANS)
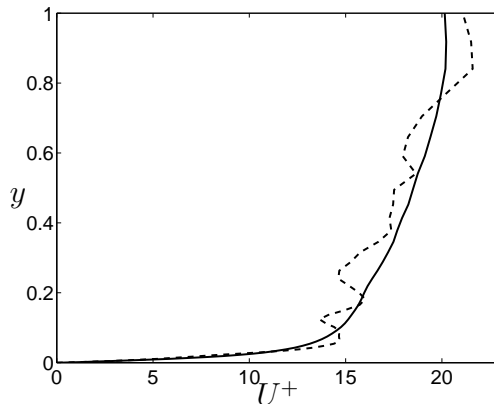
Figure 1: Velocity profiles from a DNS of channel flow. Solid line: time-averaged velocity; dashed line: instantaneous velocity.

and the large detached eddies are resolved (LES). In DES, the switch between the RANS and LES is dictated by the ratio of the RANS to the LES turbulent length scales. The latter length scale is defined from the grid (the length of the largest cell side).

The present work evaluates a new approach by Menter and co-workers [6–8] called SAS (Scale-Adapted Simulation). The SAS term is an additional production term in the ω equation that increases when the flow equations start to go unsteady. The SAS term switches itself on when the ratio of the modelled turbulent length scale, $k^{1/2}/\omega$, to the von Kármán length scale increases. The von Kármán length scale, which is based on the ratio of the first to the second velocity gradients, is smaller for an unsteady velocity profile than for a steady velocity profile, see Fig. 1. The idea of the SAS term is that, when the flow equations resolve unsteadiness, the SAS term detects the unsteadiness and increases the production of ω. The effect is that ω increases, and hence the turbulent viscosity decreases because ω appears in the denominator in the expression for ν_t and because the magnitude of the destruction term, $-\beta^* k\omega$, in the modelled turbulent kinetic energy equation increases.

The paper is organised as follows. First, the SST-SAS $k - \omega$ model is derived. In the next section, the von Kármán is evaluated using instantaneous channel data obtained by DNS (fine mesh) and hybrid LES-RANS (coarse mesh). The numerical method and the instantaneous inlet boundary conditions are then briefly presented. The results are reported and discussed, and, finally, conclusions are drawn.

2 The $k - kL$ Turbulence Model

2.1 Derivation

Rotta [9] derived an exact equation for kL based on the integral length scale.

$$kL = \frac{3}{16} \int R_{ii}(\mathbf{x}, \eta)d\eta, \quad R_{ij} = \overline{u_i(\mathbf{x})u_j(\mathbf{x} + \eta)} \tag{1}$$

All two-equation models have one production term and one destruction term. Rotta's kL equation includes two production terms, namely (here given in boundary-layer form)

$$S_{kL} = \underbrace{-\frac{3}{16}\frac{\partial \bar{u}(\mathbf{x})}{\partial y}\int R_{21}d\eta}_{I} \underbrace{-\frac{3}{16}\int \frac{\partial \bar{u}(\mathbf{x}+\eta)}{\partial y}R_{12}d\eta}_{II} \tag{2}$$

To simplify the second term, Rotta used Taylor expansion so that

$$\frac{\partial \bar{u}(\mathbf{x}+\eta)}{\partial y} = \underbrace{\frac{\partial \bar{u}(\mathbf{x})}{\partial y}}_{a} + \underbrace{\eta \frac{\partial^2 \bar{u}(\mathbf{x})}{\partial y^2}}_{b} + \underbrace{\frac{1}{2}\eta^2 \frac{\partial^3 \bar{u}(\mathbf{x})}{\partial y^3}}_{c} + \cdots \tag{3}$$

The first term, a, is incorporated in $S_{kL,I}$. Rotta set the second term, b, to zero

$$\frac{\partial^2 \bar{u}(\mathbf{x})}{\partial y^2}\int_{-\infty}^{+\infty} R_{12}\eta \, d\eta = 0 \tag{4}$$

because, in homogeneous shear flow, $R_{12}(\eta)$ is antisymmetric with respect to η. The second term in Eq. 2 was consequently modelled with the third term, c, including the third velocity gradient $\partial^3 \bar{u}/\partial y^3$.

Menter & Egorov [7] argue that homogeneous shear flow is not a relevant flow case because the second velocity gradient here is zero anyway. They propose modelling the $S_{kL,II}$ term in Eq. 2 using the second velocity gradient as [7, 8]:

$$S_{kL,IIb} = -\frac{3}{16}\int \frac{\partial \bar{u}(\mathbf{x}+\eta)}{\partial y}R_{12}d\eta = -|\overline{uv}|\left|\frac{\partial^2 \bar{u}(\mathbf{x})}{\partial y^2}\right|L^2 \tag{5}$$

The eddy-viscosity assumption for the shear stress gives $|uv| = \nu_t|\partial \bar{u}/\partial y|$. In three-dimensional flow the shear stress can be estimated by an eddy-viscosity expression, $\nu_t(2\bar{s}_{ij}\bar{s}_{ij})^{1/2}$. Using a general formula for the second derivative of the velocity we get [7, 8]

$$\begin{aligned} S_{kL,IIb} &= -\nu_t S\,|U''|\,L^2 \\ S &= (2\bar{s}_{ij}\bar{s}_{ij})^{1/2} \\ U'' &= \left(\frac{\partial^2 \bar{u}_i}{\partial x_j \partial x_j}\frac{\partial^2 \bar{u}_i}{\partial x_k \partial x_k}\right)^{1/2} \end{aligned} \tag{6}$$

In the $k - kL$ model the turbulent viscosity, ν_t, and the dissipation term, ε, in the k equation have the form

$$\nu_t = c_1 \frac{kL}{k^{1/2}} \tag{7}$$

$$\varepsilon = \frac{k^{5/2}}{kL} \tag{8}$$

3

Term $S_{kl,IIb}$ in the kL equation is a sink term that reduces kL. The result is that the turbulent viscosity is reduced because kL appears in the nominator of the expression for ν_t, see Eq. 7. This reduction is somewhat diminished since a decrease in kL also reduces k via an increase in the dissipation term, ε, see Eq. 8. However, since kL appears directly in ν_t, it is expected that the overall effect of a large $S_{kL,IIb}$ will be a decrease in ν_t.

The source term, $S_{kL,IIb}$, includes the second velocity gradient. The von Kármán length scale

$$L_{vK,1D} = \kappa \left| \frac{\partial \langle \bar{u} \rangle / \partial y}{\partial^2 \langle \bar{u} \rangle / \partial y^2} \right| \tag{9}$$

also includes the second velocity gradient. This is interesting because, as noted in [7], the von Kármán length scale decreases when the momentum equations resolve (part of) the turbulence. The von Kármán length scale is smaller for an instantaneous velocity profile than for a time-averaged velocity, see Fig. 1. When making URANS or DES, the momentum equations are triggered through instabilities to go unsteady in regions where the grid is fine enough. In URANS or in DES operating in RANS mode, high turbulent viscosity dampens out these instabilities. In many cases this is an undesired feature, because, if the flow wants to go unsteady, it is usually a bad idea to force the equations to stay steady. One reason is that there may not be any steady solution. Hence, the equations will not converge. Another reason is that, if the numerical solution wants to go unsteady, the large turbulent scales will be resolved instead of being modelled. This leads to a more accurate prediction of the flow.

The role of term $S_{kL,IIb}$ is that this term becomes large when unsteady resolved velocities appear in the flow. As discussed above, this will lead to reduced turbulent viscosity, which means that the resolved fluctuations are less likely to be dampened. This feature led Menter and co-workers [6–8] to introduce the von Kármán length scale in a one-equation model, in a $k - k^{1/2}L$ model and in a $k - \omega$ SST model. In the present study, we will use and evaluate the modified $k - \omega$ SST model.

2.2 The second derivative

To compute U'' in Eq. 6, we need to compute the second velocity gradients. In finite volume methods, there are two main options for computing second derivatives.

<u>Option I</u>: compute the first derivatives at the faces

$$\left(\frac{\partial u}{\partial y} \right)_{j+1/2} = \frac{u_{j+1} - u_j}{\Delta y}, \qquad \left(\frac{\partial u}{\partial y} \right)_{j-1/2} = \frac{u_j - u_{j-1}}{\Delta y}$$

and then

$$\Rightarrow \left(\frac{\partial^2 u}{\partial y^2} \right)_j = \frac{u_{j+1} - 2u_j + u_{j-1}}{(\Delta y)^2} + \frac{(\Delta y)^2}{12} \frac{\partial^4 u}{\partial y^4}$$

<u>Option II</u>: compute the first derivatives at the center

4

$$\left(\frac{\partial u}{\partial y}\right)_{j+1} = \frac{u_{j+2} - u_j}{2\Delta y}, \qquad \left(\frac{\partial u}{\partial y}\right)_{j-1} = \frac{u_j - u_{j-2}}{2\Delta y}$$

and then

$$\Rightarrow \left(\frac{\partial^2 u}{\partial y^2}\right)_j = \frac{u_{j+2} - 2u_j + u_{j-2}}{4(\Delta y)^2} + \frac{(\Delta y)^2}{3}\frac{\partial^4 u}{\partial y^4}$$

Option I is used in the present work unless otherwise stated.

2.3   The $k - \omega$ SST model

Now we want to transform the $S_{kL,IIb}$ term in the $k - kL$ model to the $k - \omega$ model. The kL equation (expressed in dependent variables k and kL) can be transformed term by term to the ω equation (expressed in dependent variables k and $\omega = k^{3/2}/(kL)$). The transformation reads

$$\frac{d\omega}{dt} = \frac{3}{2}\frac{k^{1/2}}{(kL)}\frac{dk}{dt} - \frac{k^{3/2}}{(kL)^2}\frac{d(kL)}{dt} \tag{10}$$

The last term is used to transform the $S_{kL,IIb}$ term (see Eq. 6) which gives

$$P_{SAS} = -\frac{k^{3/2}}{(kL)^2}\left(-\nu_t S\,|U''|\,L^2\right) = \frac{1}{k^{1/2}L}\nu_t S\,|U''|\,L \propto S\,|U''|\,L \tag{11}$$

The second velocity gradient, $\partial^2 \bar{u}/\partial y^2$, appears in the definition of the von Kármán length scale, and it is given in Eq. 9 in boundary layer form. S and U'' in Eq. 11 correspond to one form of first and second velocity gradients in three-dimensional flow. Using S and U'' in Eq. 9 and inserting these into Eq. 11 gives

$$P_{SAS} = \tilde{\zeta}_2\,S^2\frac{|U''|}{\kappa S}L = \tilde{\zeta}_2\kappa S^2\frac{L}{L_{vK,3D}}$$

$$L_{vK,3D} = \kappa\frac{S}{|U''|} \tag{12}$$

A term involving derivatives of ω appears when the $k - kL$ equation is transformed. To preserve the SST model in the URANS region, a term with derivatives of $\partial k/\partial x_i$ is also included. The final form of the additional term in the ω equation reads [8]

$$P_{SAS} = F_{SAS}\max\left(T_1 - T_2, 0\right)$$

$$T_1 = \tilde{\zeta}_2\kappa S^2\frac{L}{L_{vK,3D}}$$

$$T_2 = \frac{2k}{\sigma_\Phi}\max\left(\frac{1}{\omega^2}\frac{\partial\omega}{\partial x_j}\frac{\partial\omega}{\partial x_j}, \frac{1}{k^2}\frac{\partial k}{\partial x_j}\frac{\partial k}{\partial x_j}\right) \tag{13}$$

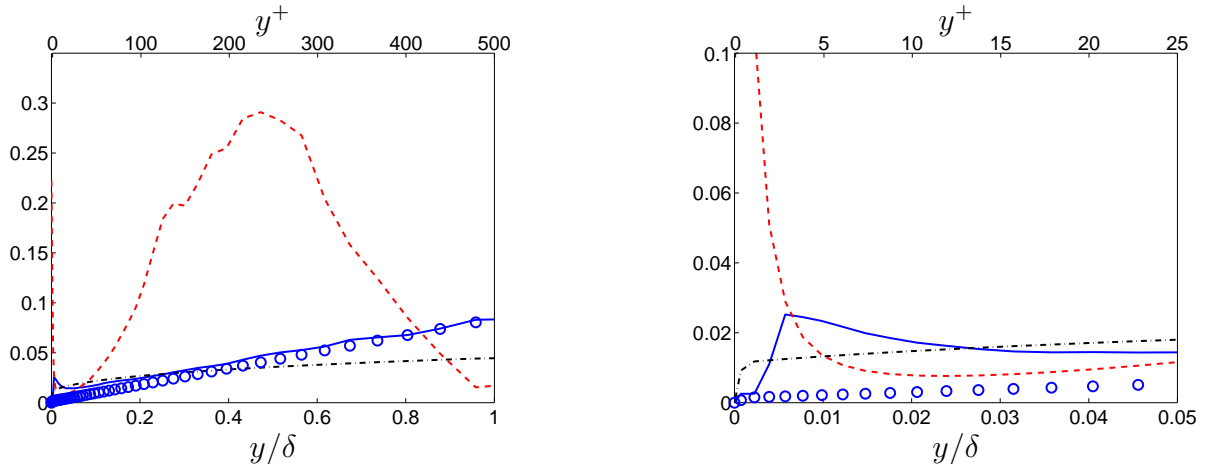$$L = \frac{k^{1/2}}{\omega c_\mu^{1/4}}$$

Figure 2: Turbulent length scales in fully developed channel flow. Left: global view; right: zoom. DNS. 96^3 mesh. $Re_\tau = 500$. $\Delta x/\delta = 0.065$, $\Delta z/\delta = 0.016$, y-stretching of 9%. —— : $\langle L_{vK,3D} \rangle$; - - - : $L_{vK,1D}$; - · - : $(\Delta x \Delta y \Delta z)^{1/3}$; ∘: Δy.

The $k - \omega$ SST-SAS can now be written

$$
\frac{\partial k}{\partial t} + \frac{\partial}{\partial x_j}(\bar{u}_j k) = \frac{\partial}{\partial x_j}\left[\left(\nu + \frac{\nu_t}{\sigma_k}\right)\frac{\partial k}{\partial x_j}\right] + P_k - \beta^* k\omega
$$

$$
\frac{\partial \omega}{\partial t} + \frac{\partial}{\partial x_j}(\bar{u}_j \omega) = \frac{\partial}{\partial x_j}\left[\left(\nu + \frac{\nu_t}{\sigma_\omega}\right)\frac{\partial \omega}{\partial x_j}\right] + P_\omega - \beta\omega^2
$$

$$
+ 2(1 - F_1)\sigma_{\omega 2}\frac{1}{\omega}\frac{\partial k}{\partial x_i}\frac{\partial \omega}{\partial x_i} + P_{SAS}
$$

$$
F = \tanh(\xi^4), \quad \xi = \min\left[\max\left\{\frac{\sqrt{k}}{\beta^* \omega y}, \frac{500\nu}{y^2\omega}\right\}, \frac{4\sigma_{\omega 2}k}{CD_\omega y^2}\right] \tag{14}
$$

$$
\nu_t = \frac{a_1 k}{\max(a_1\omega, SF_2)}, \quad P_\omega = \alpha\frac{P_k}{\nu_t}
$$

$$
F_2 = \tanh(\eta^2), \quad \eta = \max\left\{\frac{2k^{1/2}}{\beta^* \omega y}, \frac{500\nu}{y^2\omega}\right\}
$$

where CD_ω denotes the cross diffusion term.

3   Evaluation of the von Kármán length scale in fully developed channel flow

In Fig. 2 different turbulent length scales are evaluated using DNS data of fully developed channel flow. Only viscous dissipation of resolved turbulence affects the equations in DNS. This implies that the smallest scales that can be resolved are related to the grid scale. The von Kármán length scale based on instantaneous velocities, $\langle L_{vK,3D} \rangle$, is shown in Fig. 2. For $y > 0.2$, its magnitude is close to Δy, which confirms that the von Kármán length scale is related to the smallest resolvable scales. Closer to the wall, $\langle L_{vK,3D} \rangle$ increases slightly while Δy continues to decrease.
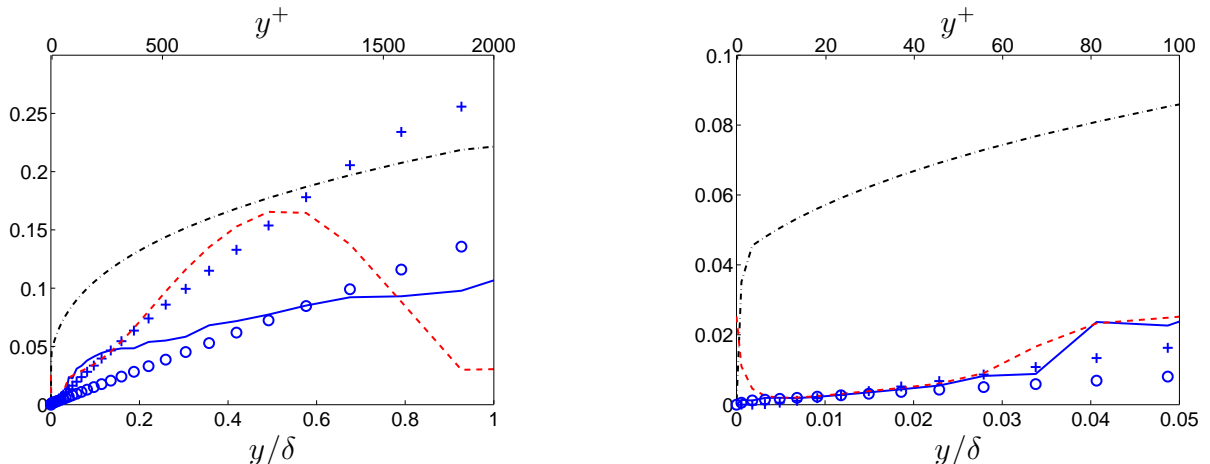
Figure 3: Turbulent length scales in fully developed channel flow. Hybrid LES-RANS. Left: global view; right: zoom. $32 \times 64 \times 32$ mesh. $Re_\tau = 2000$. $\Delta x/\delta = 0.39$, $\Delta z/\delta = 0.19$, y-stretching of 17%. —— : $\langle L_{vK,3D} \rangle$; – – – : $L_{vK,1D}$; – · – · : $(\Delta x \Delta y \Delta z)^{1/3}$; ∘: Δy; +: $\ell_{k-\omega} = k^{1/2}/(c_\mu^{1/4} \omega)$.

The von Kármán length scale, $L_{vK,1D}$ (see Eq. 9), based on the averaged velocity profile, $\langle \bar{u} \rangle = \langle \bar{u} \rangle(y)$, is also included in Fig. 2 and, as can be seen, it is much larger than $\langle L_{vK,3D} \rangle$. Near the wall, $L_{vK,1D}$ increases because the time-averaged second derivative, $\partial^2 \langle \bar{u} \rangle / \partial y^2$, goes to zero as the wall is approached. This behavior is not seen for the three-dimensional formulation, $\langle L_{vK,3D} \rangle$.

Figure 3 uses data from hybrid LES-RANS (taken from [10]). With hybrid LES-RANS, part of the turbulence is resolved and part of the turbulence is modelled. The resolved turbulence is dissipated by a modelled dissipation, $-2\langle \nu_T \bar{s}_{ij} \bar{s}_{ij} \rangle$ (ν_T denotes SGS or RANS turbulent viscosity), and $\nu_T \gg \nu$. As a result, the length scale of the smallest resolved turbulence is larger in hybrid LES-RANS than in DNS. Close to the wall in the URANS region ($y < 0.031\delta$), the resolved turbulence is dampened by the high turbulent viscosity, and, as a result, $\langle L_{vK,3D} \rangle$ follows closely $L_{vK,1D}$.

The RANS turbulent length scale, $\ell_{k-\omega}$, from a one-dimensional RANS simulation at $Re_\tau = 2000$ made with the SST model is also included in Fig. 3. In the inner region ($y < 0.5\delta$), its behavior is close to that of the von Kármán length scale, $L_{vK,1D}$. In the center region, the RANS turbulent length scale continues to increase whereas the von Kármán length scale, $L_{vK,1D}$, goes to zero.

Two filter scales are included in Figs. 2 and 3. In the DNS simulations, $\Delta y < (\Delta x \Delta y \Delta z)^{1/3}$ near the wall; far from the wall, however, $\Delta y > (\Delta x \Delta y \Delta z)^{1/3}$ because of both the stretching in the y direction and small Δx and Δz. In the hybrid simulations, it can be noted that the three-dimensional filter width is approximately twice as large as the three-dimensional formulation of the von Kármán length scale, i.e. $(\Delta x \Delta y \Delta z)^{1/3} > \langle L_{vK,3D} \rangle$.

7

4   The Numerical Method

An incompressible, finite volume code with a non-staggered grid arrangement is used [11]. For space discretization, central differencing is used for all terms. The Crank-Nicholson scheme is used for time discretization of all equations. The numerical procedure is based on an implicit, fractional step technique with a multigrid pressure Poisson solver [12].

5   Inlet Conditions

For the channel simulations inlet fluctuating velocity fields (u', v', w') are created at each time step at the inlet $y - z$ plane using synthetic isotropic fluctuations [13, 14]. These are independent of one another, however, and thus their time correlation will be zero. This is unphysical. To create correlation in time, new fluctuating velocity fields, $\mathcal{U}'$, $\mathcal{V}'$, $\mathcal{W}'$, are computed as [13, 15, 16]

$$
\begin{aligned}
(\mathcal{U}')^m &= a(\mathcal{U}')^{m-1} + b(u')^m \\
(\mathcal{V}')^m &= a(\mathcal{V}')^{m-1} + b(v')^m \\
(\mathcal{W}')^m &= a(\mathcal{W}')^{m-1} + b(w')^m
\end{aligned}
\tag{15}
$$

where m denotes time step number, $a = \exp(-\Delta t/\mathcal{T})$ and $b = (1 - a^2)^{1/2}$. The time correlation of $\mathcal{U}'_i$ will be equal to $\exp(-\Delta t/\mathcal{T})$, where $\mathcal{T}$ is proportional to the turbulent time scale. The inlet boundary conditions are prescribed as

$$
\begin{aligned}
\bar{u}(0, y, z, t) &= U_{in}(y) + u'_{in}(y, z, t) \\
\bar{v}(0, y, z, t) &= v'_{in}(y, z, t) \\
\bar{w}(0, y, z, t) &= w'_{in}(y, z, t)
\end{aligned}
\tag{16}
$$

The mean inlet velocity, $U_{in}(y)$, k and ω are taken from one-dimensional channel flow predicted with the SST model.

For the diffuser flow simulations, the inlet conditions are taken from a DNS of fully developed channel flow at $Re_\tau = 500$. k and ω are taken from one-dimensional channel flow obtained with the SST model.

For the three-dimensional hill simulations, fluctuations are taken from the same DNS of channel flow. These fluctuations are then re-scaled and superimposed on the experimental mean inlet velocity profile. Neumann conditions are used for k and ω.

6   Results

6.1   Channel Flow

A $256 \times 64 \times 32$ node mesh (x, streamwise; y, wall-normal; z, spanwise) was used. The size of the computational domain is $x_{max} = 100$, $y_{max} = 2$ (geometric stretching of 17%) and $z_{max} = 6.28$, see Fig. 4. This gives a Δx^+ and Δz^+ of approximately 785 and 393, respectively, and $y^+ < 1$ near the walls, expressed in inner scaling. In outer scaling,
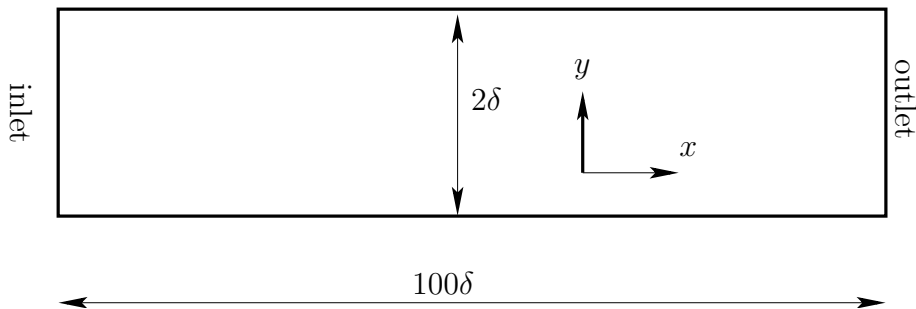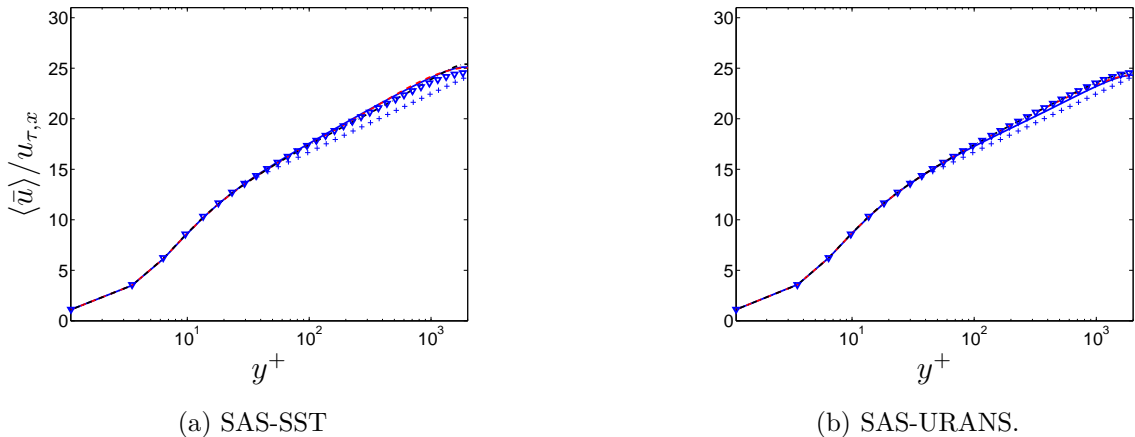
PSfrag replacements

inlet

outlet

2δ

y

x

100δ

Figure 4: Channel with inlet and outlet.

PSfrag replacements

$\langle \bar{u} \rangle / u_{\tau,x}$

y^+

PSfrag replacements

y^+

(a) SAS-SST

(b) SAS-URANS.

Figure 5: Velocity profiles. —— : $x/\delta = 3.33$; - - - : $x/\delta = 23$; - · - : $x/\delta = 97$; +: $2.5\ln(y^+) + 5.2$; $\triangledown$: from a 1D simulation with the SST model.

$\delta/\Delta x \simeq 2.5$ and $\delta/\Delta z \simeq 5$. The time step was set to $\Delta t u_\tau/\delta = 4.91 \cdot 10^{-3}$. The Reynolds number is $Re_\tau = u_\tau \delta/\nu = 2000$. Neumann boundary conditions are prescribed at the outlet.

The results using the standard SST-URANS model and the SST-SAS model are presented below. Figure 5 shows the velocity profiles; the results obtained with the two models are very similar. Figures 6 and 7 show the predicted resolved Reynolds stresses. As can be seen, the stresses predicted by the SST-SAS model decay at a slower rate than those predicted by the SST-URANS model. The reason is that the turbulent viscosity is smaller with the SST-SAS model than with the SST-URANS model (Fig. 8), which makes the dissipation of the resolved fluctuations smaller with the former model. It can be noted that, at the end of the channel ($x/\delta = 97$), the turbulent viscosity obtained with the SST-URANS model is equal to the turbulent viscosity predicted in a one-dimensional channel using the SST-URANS model (see Fig. 8b) and that the resolved stresses are zero. Hence, the flow has returned to fully steady conditions.
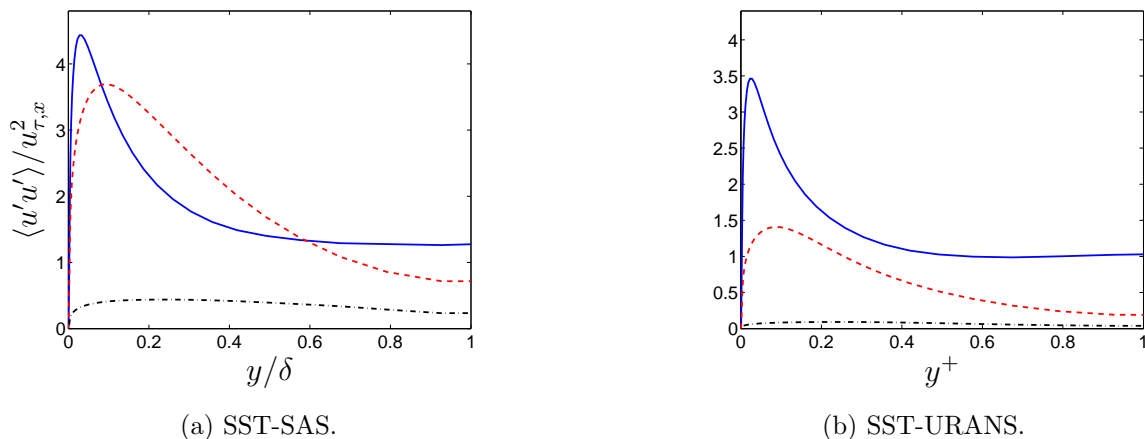
9

(a) SST-SAS.

(b) SST-URANS.

Figure 6: Streamwise resolved normal stresses. —— : $x/\delta = 3.33$; – – – : $x/\delta = 23$; – · – : $x/\delta = 97$.
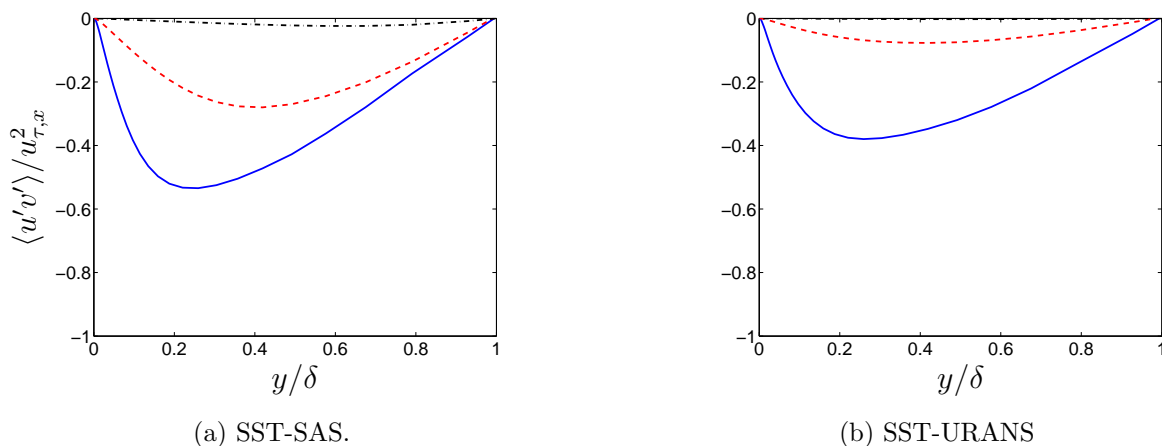

(a) SST-SAS.

(b) SST-URANS

Figure 7: Resolved shear stresses. —— : $x/\delta = 3.33$; – – – : $x/\delta = 23$; – · – : $x/\delta = 97$.

Figure 9a presents the ratio of the turbulent length scale, $L = k^{1/2}/(c_\mu^{1/4}\omega)$, to the von Kármán length scale. As expected, the von Kármán is largest near the inlet, where the resolved fluctuations are largest. Near the inlet, the von Kármán length scale is more than twice as large as the turbulent length scale, L. When the resolved stresses far downstream become very small (i.e. the flow goes towards a steady solution), the ratio near the centerline increases since the von Kármán length scale for steady flow is small in this region, cf. Fig. 3a.

The ratio of the production term, P_ω, to the SAS term, P_{SAS}, in the ω equation is presented in Fig. 9b. The SAS term is large near the inlet, more than three times P_ω, and it decreases further downstream as the resolved fluctuations are dampened.
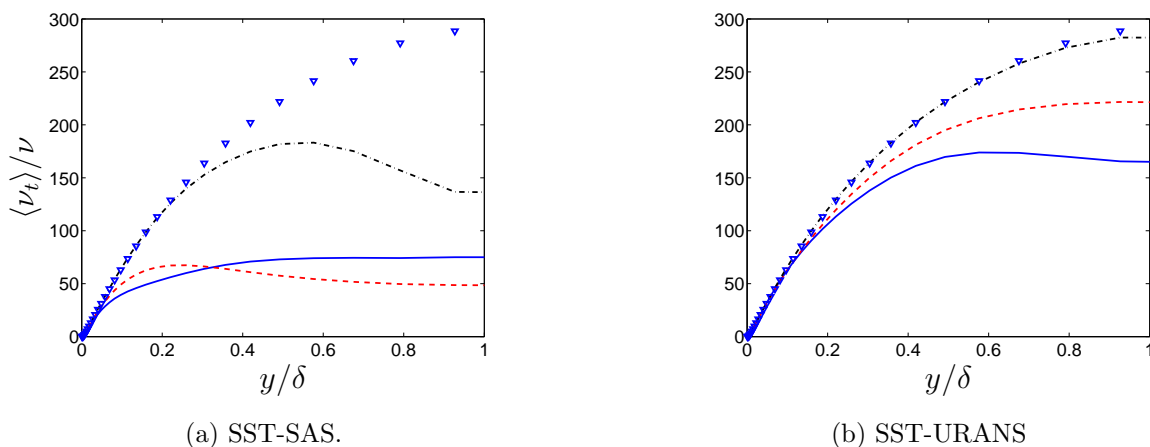
10

(a) SST-SAS.

(b) SST-URANS

Figure 8: Turbulent viscosity. —— : $x/\delta = 3.33$; - - - : $x/\delta = 23$; - - - : $x/\delta = 97$; $\bigtriangledown$: from a 1D simulation with the SST model.

(a) Ratio of turbulent length scales.
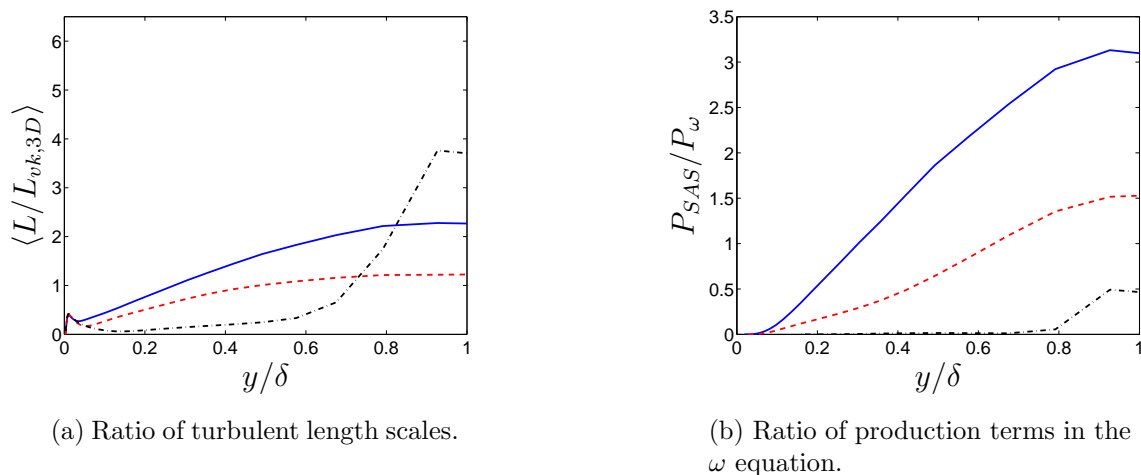
(b) Ratio of production terms in the ω equation.

Figure 9: SAS-SST model. SAS terms. —— : $x/\delta = 3.33$; - - - : $x/\delta = 23$; - - - : $x/\delta = 97$.

Figure 10 shows the maximum of the resolved stresses vs. x. Here it is again illustrated that the resolved stresses are dampened much faster with the SST-URANS model than with the SST-SAS model.

The friction velocities are presented in Fig. 11. In the developing unsteady region, the friction velocity differs from its steady-state value of one and, as the resolved fluctuations are dampened further downstream, the friction velocity approaches one.
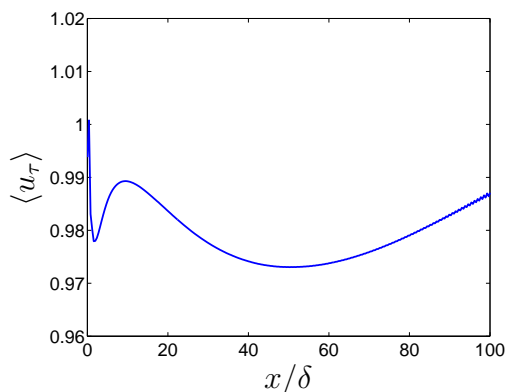
Figure 12 gives the maximum of the resolved stresses vs. x. Options I and II for computing the second velocity derivatives in U'' (see Section 2.2) are compared. Option
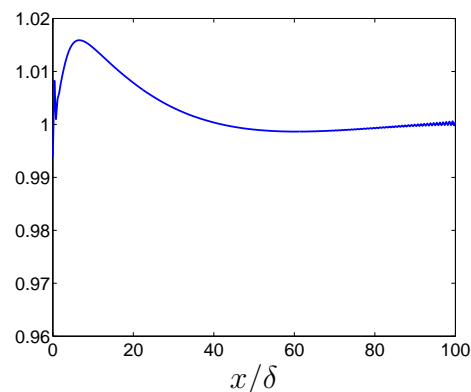
11
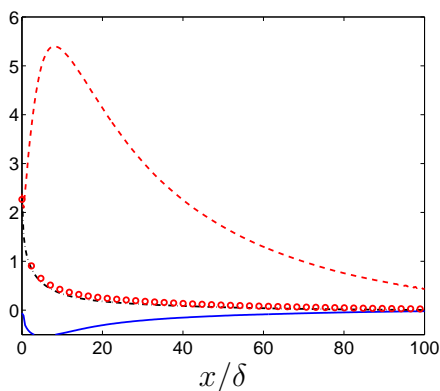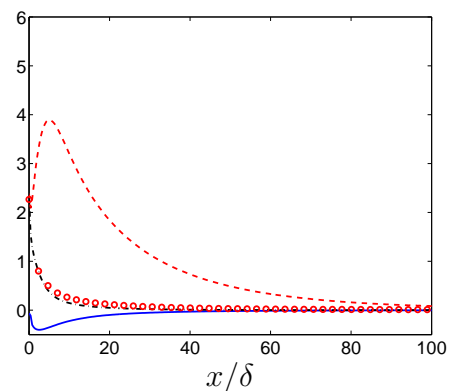
(a) SST-SAS.

(b) SST-URANS

Figure 10: Decay of resolved stresses. ——: $\langle u'v'\rangle/u_{\tau,x}^2$; – – –: $\langle u'u'\rangle/u_{\tau,x}^2$; –·–: $\langle v'v'\rangle/u_{\tau,x}^2$; ○: $\langle w'w'\rangle/u_{\tau,x}^2$.

(a) SST-SAS.

(b) SST-URANS

Figure 11: Friction velocities.

II uses only every second node, and hence U'' becomes larger (P_{SAS} smaller) than with Option I. As a result, the turbulent viscosity is smaller with Option I as compared with Option II, and this explains why the resolved stresses are larger with Option I than with Option II, see Figure 12.

6.2   Asymmetric Diffuser

The configuration is an asymmetric plane diffuser, see Fig. 13a, with Reynolds number $Re = U_{b,in}H/\nu = 18\,000$ ($U_{b,in} = H = 1$). The opening angle is 10°. Periodic boundary conditions are prescribed in the spanwise direction. The mesh has $256 \times 64 \times 32$
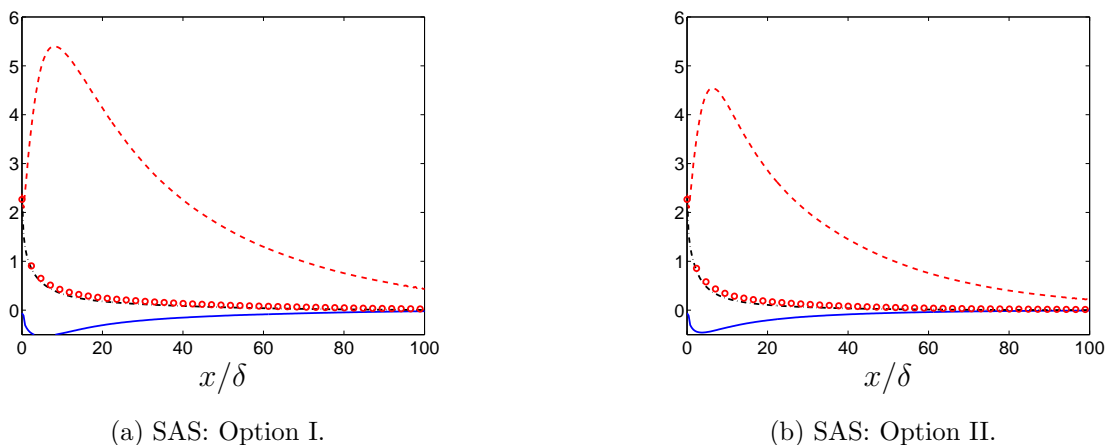
12

(a) SAS: Option I.

(b) SAS: Option II.

Figure 12: SAS model. Decay of resolved stresses. Two different options for computing the second velocity derivatives, see Section 2.2. ——: $\langle u'v'\rangle/u_{\tau,x}^2$; – – –: $\langle u'u'\rangle/u_{\tau,x}^2$; – · – : $\langle v'v'\rangle/u_{\tau,x}^2$; ○: $\langle w'w'\rangle/u_{\tau,x}^2$.

(a) Plane asymmetric diffuser (not to scale). The spanwise width is $z_{max} = 4H$.

(b) Three-dimensional hill. Origin of the coordinate system is located at the lower wall at the center of the hill.
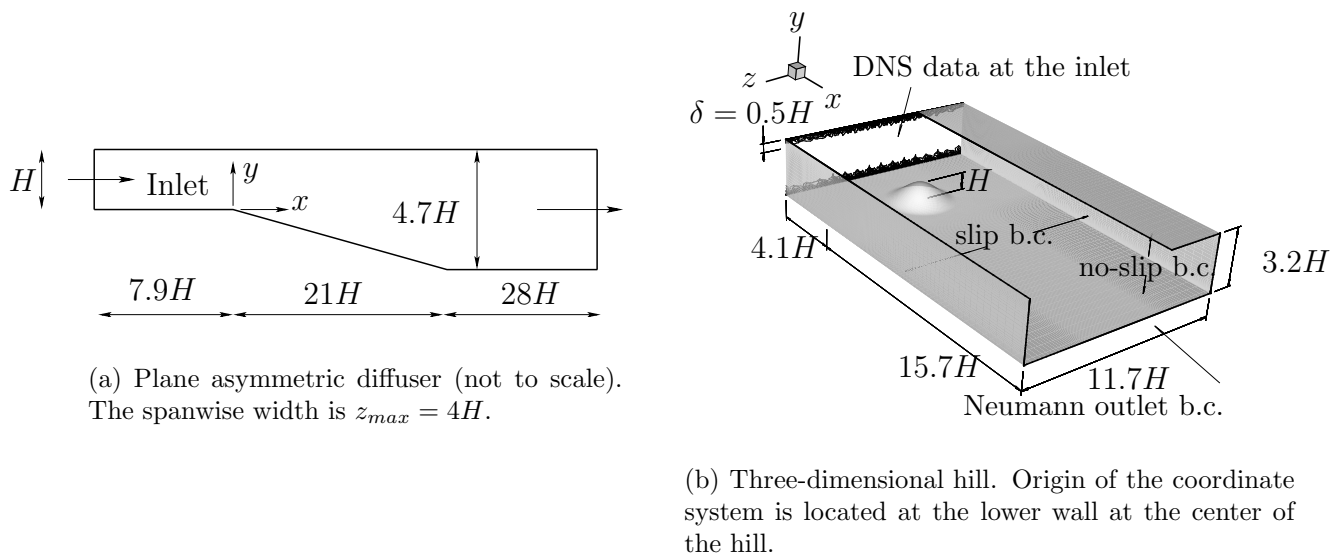
Figure 13: Configurations.

(x, y, z) cells (body-fitted, structured, nearly orthogonal mesh). The CPU time is approximately $10s$ per time step on a Linux PC (AMD Opteron 246). A time step of 0.04 is used ($CFL_{max} \simeq 1$), and two global iterations are needed at each time step to reach convergence.

The velocity profiles are presented in Fig. 14 and it can be seen that the agreement with experiments is better for the SST-URANS model than for the SST-SAS model. The reason is that the turbulent viscosity is reduced by the SAS term, which allows part of the
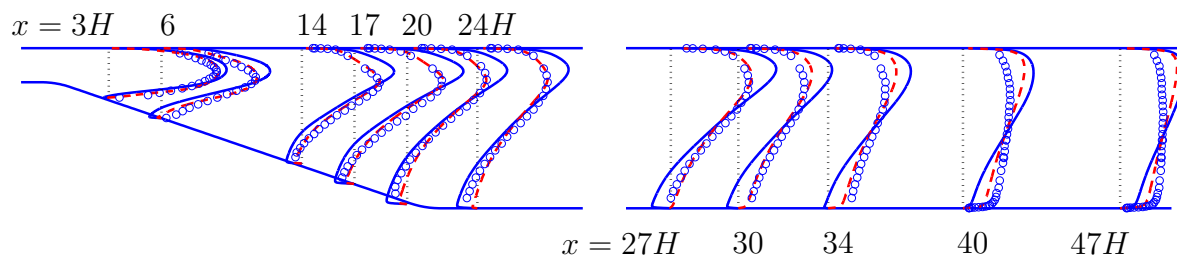
$x = 3H \quad 6 \qquad 14 \quad 20 \quad 24H$

$x = 27H \quad 30 \quad 34 \qquad 40 \qquad 47H$

Figure 14: Diffuser (not to scale). $\langle \bar{u} \rangle$-velocities. —— : SST-SAS; - - - : SST-URANS; markers: experiments [17].
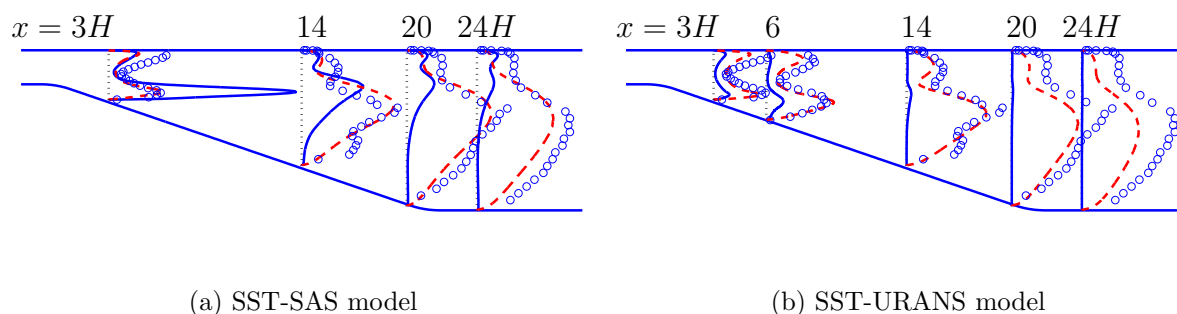
$x = 3H \qquad 14 \quad 20 \quad 24H$

6

17

$x = 3H \quad 6 \qquad 14 \quad 20 \quad 24H$

17

(a) SST-SAS model

(b) SST-URANS model

Figure 15: Diffuser (not to scale). Normal stresses. —— : $\langle u'^2 \rangle$; - - - : $2k/3$; markers: experiments [17].

$x = 3H \quad 6 \qquad 14 \ 17 \ 20 \ 24H$

(a) Turbulent viscosity, $\langle \nu_t \rangle / \nu$. —— : SAS-SST; - - - : SAS-URANS.

(b) Ratio of SAS term to production term, P_{sas}/P_ω, in the ω equation.
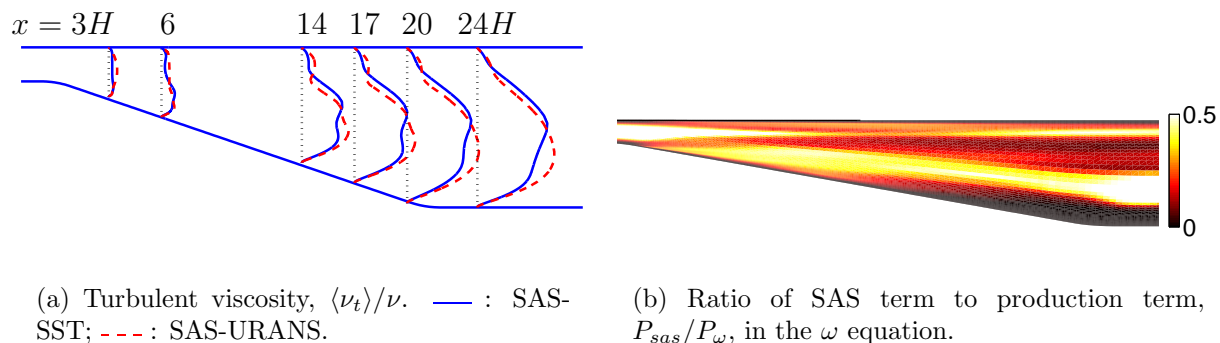
Figure 16: Diffuser.

turbulence to be resolved. The problem is that the resolved turbulence is only partially triggered, and it decays in the diffuser part; at the end of the diffuser part, $x/H = 24$, (see Fig. 15a) it has vanished completely in the lower half of the diffuser and is small in the upper half. With the SST-URANS model the resolved turbulence is already damped out at $x/H = 14$, see Fig. 15b. The modelled turbulent kinetic energy, k, is also larger with the SST-SAS model than with the SST-URANS model. This can probably be explained by the larger production term in the former case, since part of the turbulence is resolved with the SST-SAS model which yields a large strain rate $\bar{s}_{ij}\bar{s}_{ij}$ in P_k. The turbulent viscosity is

(a) Zoom of the grid. Every second grid lines is shown.

(b) Experiments

(c) SST-SAS model
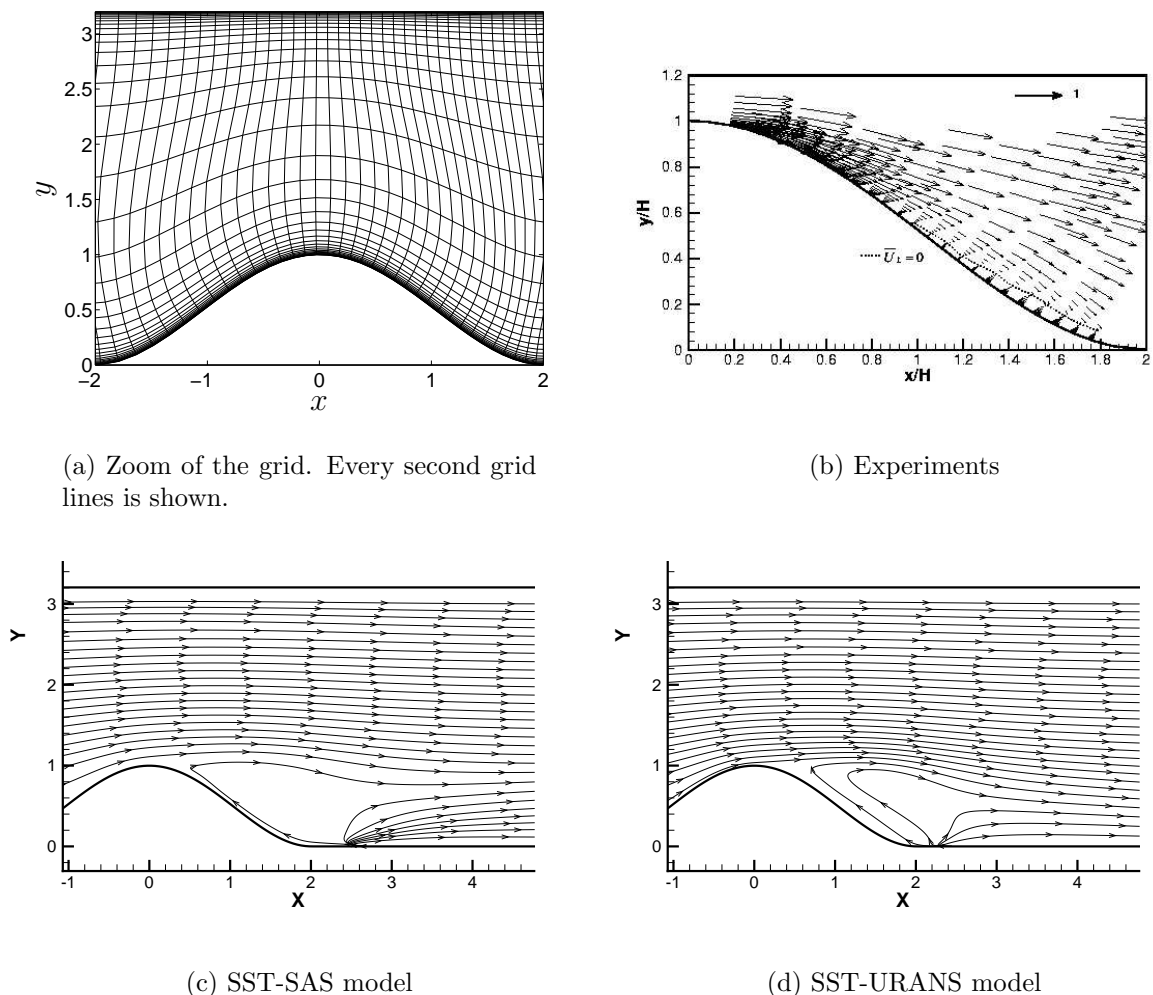
(d) SST-URANS model

Figure 17: Three-dimensional hill. Grid and streamlines in the center plane $z = 0$.

smaller with the SST-SAS model than with the SAS-URANS model (Fig. 16a), however, and this is due to a larger ω because of the SAS term in the ω equation. The ratio of the SAS term to the usual production term is shown in Fig. 16b, and it can be seen that the SAS term is largest below the center of the diffuser. As expected, this corresponds to the region where the turbulent viscosity predicted by the SAS-SST model is smaller than that predicted by the SAS-URANS model ($14 \leq x/H \leq 24$, see Fig. 16a)

6.3 Three-Dimensional Hill

A $162 \times 82 \times 130$ (x, y, z) mesh is used (1.7 million cells). It is nearly orthogonal in the near-wall region of the hill, see Fig. 17a. The inlet is located at $x = -4.1H$ and the outlet at $x = 15.7H$, see Fig. 13b. Periodic conditions are used at the side walls and
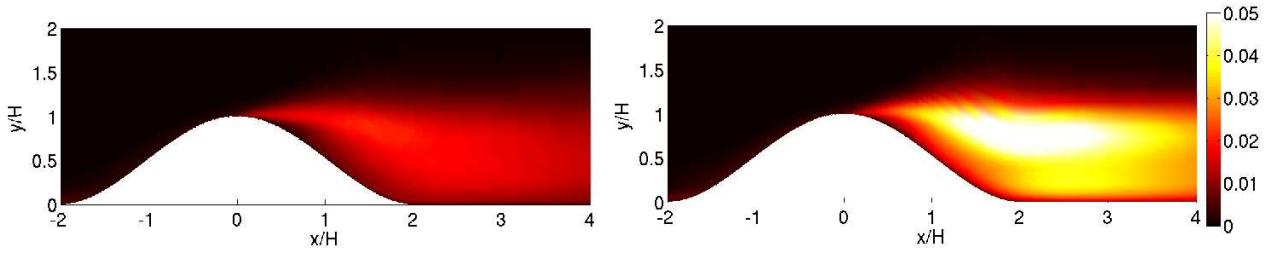
(a) SST-SAS model.
(b) SST-URANS model.
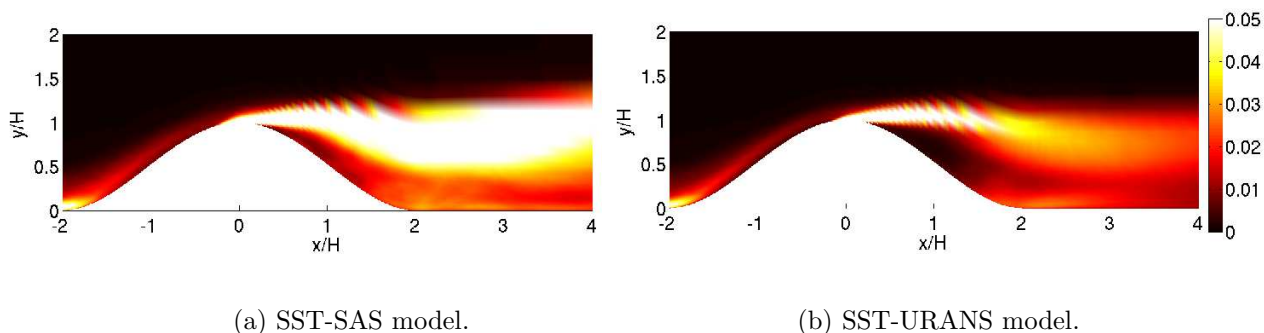
Figure 18: Three-dimensional hill. Resolved normal stress $\langle u'u' \rangle / U_{b,in}^2$. $z = 0$.

(a) SST-SAS model.
(b) SST-URANS model.
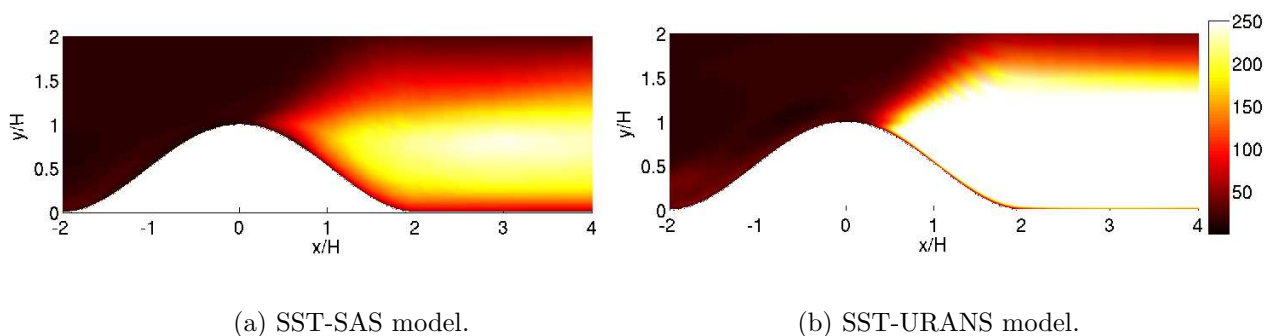
Figure 19: Three-dimensional hill. Turbulent viscosity, $\langle \nu_t \rangle / \nu$. $z = 0$.

homogeneous Neumann conditions are employed for all variables at the outlet.

The streamlines in the center plane are compared with experiments in Fig. 17b-d. The predicted height of the recirculating region is close to H for both models whereas the corresponding height in the experiments is approximately $0.1H$. This is similar to what was found in the Flomania project [18] where all steady RANS simulations gave a recirculation region similar to that shown in Fig. 17c-d.

The resolved streamwise normal stresses are presented in Fig. 18. The resolved fluctuations with the two models are similar upstream of the crest of the hill, but are much larger downstream of the crest with the SST-SAS model than with the SST-URANS model, especially some distance away from the wall ($y/H \simeq 0.8$). It can be noted that the ratio of the resolved turbulence to the modelled turbulence is larger here than for the diffuser flow.

Figure 19 and 20 present the turbulent viscosity and the modelled turbulent kinetic energy. As was found for the diffuser flow, the predicted turbulent viscosity is smaller with the SST-SAS model than with the SST-URANS model. The predicted turbulent kinetic

16

(a) SST-SAS model.

(b) SST-URANS model.

Figure 20: Three-dimensional hill. Modelled turbulent kinetic energy, k/U_{in}^2. $z = 0$.
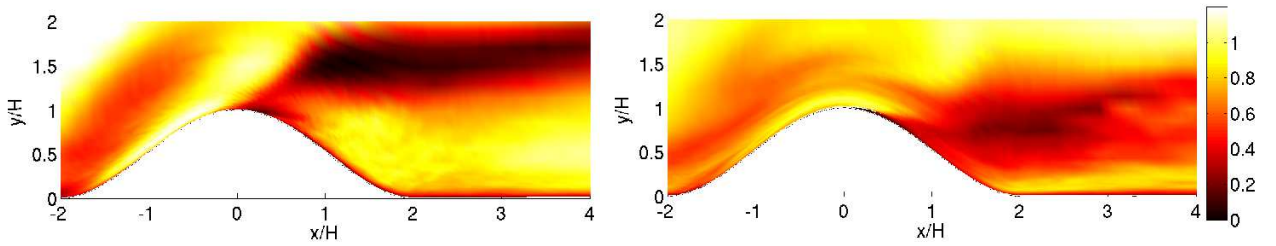
(a) $z = 0$

(b) $z = 1.13H$

Figure 21: Three-dimensional hill. Ratio of SAS term to production term, P_{sas}/P_ω, in the ω equation. $z = 0$

17

(a) Resolved normal stress $\langle u'u' \rangle / U_{b,in}^2$.

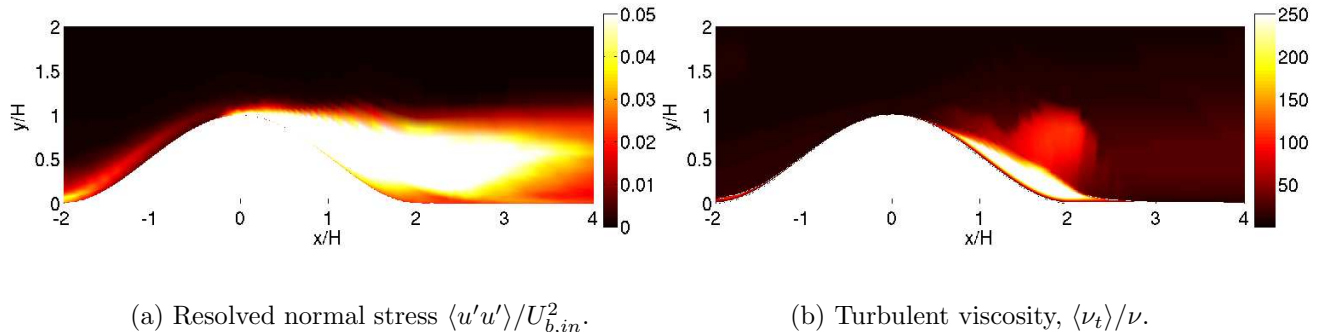(b) Turbulent viscosity, $\langle \nu_t \rangle / \nu$.

Figure 22: Three-dimensional hill. Predictions with a hybrid LES-RANS with forcing [19]. $z = 0$.

energy is, contrary to the diffuser flow, smaller with the SST-SAS model than with the SST-URANS model. The reason is probably that the SAS term plays a larger role here compared to the diffuser flow. The ratio of the SAS term to the usual production term is close to one in a large region in Fig. 21, whereas in the diffuser flow it is mostly smaller than 0.5, see Fig. 16.

In [19] this flow was computed using hybrid LES-RANS (with forcing) using the same code and the same mesh as in the present study. The predicted results were in reasonable agreement with experiments. The resolved streamwise stress and the turbulent viscosity are shown in Fig. 22. The magnitude of the resolved streamwise stress is similar for the hybrid LES-RANS (Fig. 22a) and the SST-SAS model (Fig. 18a), but the maximum is located slightly closer to the wall in the former case. However, the turbulent viscosity predicted by the hybrid LES-RANS (Fig. 22b) is much smaller than is predicted by the SST-SAS model (Fig. 19a).

7 Conclusions

The SST-SAS model was compared with the standard SST-URANS model in channel flow, diffuser flow and the flow over a three-dimensional hill. Unsteady, turbulent inlet boundary conditions are prescribed in both cases. It was confirmed that the SAS term acts as expected: it reduces the turbulent viscosity compared to the SST-URANS model and the resolved fluctuations are much larger with the SST-SAS model than with the SST-URANS model.

The grid used in the channel flow simulations is very coarse ($\delta/\Delta x = 2.5$ and $\delta/\Delta z = 5$, where δ denotes half-channel width). Hence, resolved turbulent fluctuations can not be sustained with any of the models. The damping of resolved turbulence by the coarse grid and the relatively large turbulent viscosities are too large. The prescribed turbulent fluctuations in the channel flow decay at a much slower rate with the SAS-SST model than with the SAS-URANS model.

The flow in the asymmetric diffuser is adversely affected by the SAS term. The flow

predicted with the SST-SAS model is in poorer agreement than that predicted with the SST-URANS model. The SAS term in the ω equation partly triggers resolved turbulence by reducing the turbulent viscosity. The problem is that the turbulent viscosity stays too large and, as a result the equations operate neither in RANS mode nor in LES/URANS mode but somewhere in between. With the SST-URANS, the imposed fluctuation at the inlet decays in the throat of the diffuser and the predicted flow in the main part of the diffuser is steady.

The flow around the axi-symmetric hill is poorly predicted by both models. The predicted recirculating region in the center plane is much too large compared with experiments. On the lee-side of the hill a rather large unsteadiness prevails in both models, but the resolved fluctuations are larger with the SST-SAS model than with the SST-URANS model. However, when compared with hybrid LES-RANS – which does give a flow field in reasonable agreement with experiments – the turbulent viscosity predicted with the two models is much too large.

The SAS term is expressed as the ratio of the von Kármán length scale, $L_{vk,3D}$, to the usual RANS turbulent length scale, $c_\mu^{-1/4}k^{1/2}/\omega$. The von Kármán length scale is evaluated using data from a DNS simulation and from a hybrid LES-RANS simulation. It is found that when the DNS data are used the von Kármán length scale expressed in instantaneous velocity gradients closely follows the smallest grid spacing, i.e. the wall-normal spacing, Δy. When the hybrid LES-RANS data are used the von Kármán length scale in the wall region (i.e. the URANS region) is slightly larger than Δy because of rather larger turbulent viscosities, which make the smallest, resolved scales larger.

The concept of using the von Kármán turbulent length scale for detecting unsteadiness is very interesting. This idea should be pursued further and could be used in connection with other models. In the SST-SAS model the von Kármán length scale is used to trigger an additional source term. As an alternative it could probably also be used to change the value of a coefficient in a transport turbulence model.

REFERENCES

[1] R. Franke and W. Rodi. Calculation of vortex shedding past square cylinders with various turbulence models, 8th turbulent shear flow. In *8th Symp. on Turbulent Shear Flows*, pages 20:1:1 – 20:1:6, Munich, 1991.

[2] G. Bosch and W. Rodi. Simulation of vortex shedding past a square cylinder with different turbulence models. *International Journal for Numerical Methods in Fluids*, 28(4):601–616, 1998.

[3] S. Johansson, L. Davidson, and E. Olsson. Numerical simulation of vortex shedding past triangular cylinders at high Reynolds number. *Int. J. Numer. Meth. Fluids*, 16:859–878, 1993.

[4] P.R. Spalart, W.-H. Jou, M. Strelets, and S.R. Allmaras. Comments on the feasability of LES for wings and on a hybrid RANS/LES approach. In C. Liu and Z. Liu, editors,

Advances in LES/DNS, First Int. conf. on DNS/LES, Louisiana Tech University, 1997. Greyden Press.

[5] A. Travin, M. Shur, M. Strelets, and P. Spalart. Detached-eddy simulations past a circular cylinder. *Flow Turbulence and Combustion*, 63(1/4):293–313, 2000.

[6] F.R. Menter, M. Kuntz, and R. Bender. A scale-adaptive simulation model for turbulent flow prediction. AIAA paper 2003–0767, Reno, NV, 2003.

[7] F.R. Menter and Y. Egorov. Revisiting the turbulent length scale equation. In *IUTAM Symposium: One Hundred Years of Boundary Layer Research*, Göttingen, 2004.

[8] F.R. Menter and Y. Egorov. A scale-adaptive simulation model using two-equation models. AIAA paper 2005–1095, Reno, NV, 2005.

[9] J.C. Rotta. *Turbulente Strömungen*. Teubner Verlag, Stuttgart, 1972.

[10] L. Davidson and S. Dahlström. Hybrid LES-RANS: An approach to make LES applicable at high Reynolds number. *International Journal of Computational Fluid Dynamics*, 19(6):415–427, 2005.

[11] L. Davidson and S.-H. Peng. Hybrid LES-RANS: A one-equation SGS model combined with a $k - \omega$ model for predicting recirculating flows. *International Journal for Numerical Methods in Fluids*, 43:1003–1018, 2003.

[12] P. Emvin. *The Full Multigrid Method Applied to Turbulent Flow in Ventilated Enclosures Using Structured and Unstructured Grids*. PhD thesis, Dept. of Thermo and Fluid Dynamics, Chalmers University of Technology, Göteborg, 1997.

[13] M. Billson. *Computational Techniques for Turbulence Generated Noise*. PhD thesis, Dept. of Thermo and Fluid Dynamics, Chalmers University of Technology, Göteborg, Sweden, 2004.

[14] L. Davidson and M. Billson. Hybrid LES/RANS using synthesized turbulence for forcing at the interface (in print). *International Journal of Heat and Fluid Flow*, 2006.

[15] M. Billson, L.-E. Eriksson, and L. Davidson. Jet noise prediction using stochastic turbulence modeling. AIAA paper 2003-3282, 9th AIAA/CEAS Aeroacoustics Conference, 2003.

[16] L. Davidson. Hybrid LES-RANS: Inlet boundary conditions. In *3rd National Conference on Computational Mechanics – MekIT'05 (invited paper)*, Trondheim, Norway, 2005.

[17] C.U. Buice and J.K. Eaton. Experimental investigation of flow through an asymmetric plane diffuser. Report No. TSD-107, Thermosciences Division, Department of Mechanical Engineering, Stanford University, Stanford, California 94305, 1997.

[18] W. Haase, B. Aupoix, U. Bunge, and D. Schwamborn, editors. *FLOMANIA: Flow-Physics Modelling – An Integrated Approach*, volume 94 of *Notes on Numerical Fluid Mechanics and Multidisciplinary Design*. Springer, 2006.

[19] L. Davidson and S. Dahlström. Hybrid LES-RANS: Computation of the flow around a three-dimensional hill. In W. Rodi and M. Mulas, editors, *Engineering Turbulence Modelling and Measurements 6*, pages 319–328. Elsevier, 2005.